


Exploring the Relation Between Magnetic Fields, Starspots, and CMEs

Fabian Menezes¹ , Adriana Valio², Yuri Netto¹, Alexandre Araújo¹,
Christina Kay³ and Merav Opher⁴

¹Universidade Presbiteriana Mackenzie, Centro de Rádio Astronomia e Astrofísica Mackenzie (CRAAM), São Paulo, Brazil
email: menezes.astroph@gmail.com

²Universidade de São Paulo, Instituto de Astronomia, Geofísica e Ciências Atmosféricas (IAG), Departamento de Astronomia, São Paulo, Brazil

³NASA Goddard Space Flight Center, Heliophysics Science Division, Greenbelt, USA

⁴Boston University, Department of Astronomy, Boston, USA

Abstract. Solar-type stars, including the Sun, have magnetic fields that extend from their interiors to the surface and beyond, influencing both the stellar activity and interplanetary medium. Magnetic activity phenomena, such as coronal mass ejections (CMEs), significantly impacts space weather. These CMEs, composed of plasma clouds with magnetic fields ejected from the stellar corona, pose a potential threat to planets by affecting their magnetosphere and atmosphere. Despite advancements in detecting stellar CMEs, detection remains limited. We focus on understanding CME propagation by analyzing key parameters like position, velocities, and the configuration of stellar magnetic fields. Using spot transit mapping, we reconstruct magnetograms for Kepler-63 and Kepler-411, employing the ForeCAT model to simulate CME trajectories from these stars. Results indicate that CME deflections generally decrease with radial velocity and increase with ejection latitude. Additionally, stars with stronger magnetic fields, such as Kepler-63, tend to cause more significant CME deflections.

Keywords. Solar-type stars; Starspots; Stellar magnetic field; coronal mass ejections (CMEs)

1. Introduction

The Sun and other stars have magnetic fields that permeate their interiors and affects their evolution in many ways, according to [Brun and Browning \(2017\)](#). According to [Parker \(1955\)](#); [Spruit \(1997\)](#); [Spruit et al. \(2010\)](#); [Charbonneau \(2014\)](#) and [Stejko et al. \(2020\)](#), stellar magnetic fields originate in the depths of the convective zone of the star, specifically in the tachocline. The solar dynamo theory explains the formation of these magnetic field concentrations, initiated in the tachocline and amplified in the convective zone. Magnetic flux tubes, forming in the tachocline, float towards the photosphere due to the pressure of their intense magnetic fields. These flux tubes eventually emerge into the photosphere, giving rise to areas of concentrated magnetic field, observable as sunspots and faculae. These features serve as indicators of solar magnetic activity and topology.

Stellar magnetic activity also manifests itself as starspots and coronal mass ejections (CMEs). Starspots are cooler regions on the photosphere of stars, formed by concentrations of magnetic field. The relation between starspots and CMEs is complex and understanding it is important for predicting and mitigating the impacts of stellar activity on orbiting planets. In the case of the Sun, the most impactful events in space weather

are CMEs – confined plasma clouds with a magnetic field ejected from the solar corona (Gopalswamy et al. 2009), that can cause geomagnetic storms on Earth. The study of starspots, magnetic fields, and CMEs helps unravel the dynamics of stars and their impact on space weather.

Studies by Cremades and Bothmer (2004); Kilpua et al. (2009), and Gopalswamy et al. (2009) indicate that CMEs often deflect towards local null points in the magnetic field, directed away from coronal holes. The heliospheric current sheet, marking the solar magnetic field's polarity shift, plays a crucial role. The complexity of the sheet's configuration during the solar cycle can impact CME trajectories, leading to increased deflections. Notably, slow CMEs tend to follow a deflection pattern towards the streamer belt, while fast CMEs exhibit less correlation. Kay et al. (2013, 2015) contributed to space weather predictions by developing ForeCAT, a model based on magnetohydrodynamics. ForeCAT considers magnetic forces, deflection, and rotation of CMEs, emphasizing their tendencies to deflect towards the heliospheric current sheet on a global scale, with significant deflection occurring closer to the Sun.

The extrasolar space weather can significantly differ from the space weather in the Solar System, as exoplanets may orbit a star at much closer distances, where stellar activity and magnetic field strength can be much higher. In stars with strong magnetic activity, planets in orbit may be subjected to more extreme space weather compared to Earth. The star's UV radiation, as well as the action of an intense stellar wind and the frequent impact of CMEs, can subject a planet to atmospheric erosion. This can result in a planetary surface exposed to ionizing radiation, which is harmful to biological organisms, as evidenced by Estrela and Valio (2018) and Estrela et al. (2020). In a study using the ForeCAT model and combining knowledge of the Solar System's space weather with inferred properties from other systems to study the trajectory of hypothetical CMEs launched into the interplanetary medium, Kay et al. (2016) analyzed the probability of CMEs reaching exoplanets. The authors found that this probability decreases with an increase in the inclination of the planetary orbit concerning the astrospheric current sheet.

In Menezes et al. (2023), we combined the knowledge of the space weather in the Solar System with inferred properties from other systems to reconstruct magnetograms (magnetic field maps of the photosphere) and study the trajectory of hypothetical CMEs launched into the interplanetary medium from the stars Kepler-63 and Kepler-411. Both stars exhibit strong magnetic activity (Sanchis-Ojeda et al. 2013; Sun et al. 2019) and are solar-type stars, *i.e.* FGK spectral type main-sequence stars (Izidoro et al. 2017). Also, we use solar model cases for comparison. In this present work, our primary focus is directed towards the reconstruction of magnetograms for these stars and how their topology affect the results obtained in Menezes et al. (2023).

2. Kepler Stars

Kepler-63 and Kepler-411, both exhibiting strong magnetic activity, are young stars with ages of approximately 210 ± 35 Myr and 212 ± 31 Myr, respectively (Sanchis-Ojeda et al. 2013; Estrela and Valio 2016; Sun et al. 2019; Netto and Valio 2020; Araújo and Valio 2021). Kepler-411 is a young solar-type K2V star, hosting at least 3 transiting planets (Sun et al. 2019; Araújo and Valio 2021). Kepler-63, a G-type star, has a significantly shorter magnetic activity cycle than the solar cycle, with a period of 1.27 years, and hosts a gas giant, Kepler-63b, in an almost polar orbit with respect to the star's rotation axis (Sanchis-Ojeda et al. 2013; Netto and Valio 2020).

It is worth noting that the age of a star plays a crucial role in determining various aspects, including the strength and configuration of its magnetic field, rotation, activity, and mass loss, as indicated by studies such as Skumanich (1972); Wood et al. (2002);

Charbonneau (2014); Morris (2020). Despite the relatively young age of Kepler-63 and Kepler-411, as discussed in Menezes *et al.* (2023), we regard them as comparable to the Sun. Consequently, we standardize the input parameters to match those of the Sun, encompassing the density and velocity of the stellar wind, the shape, size, expansion, mass, and velocity of CMEs, the source-surface height of the background magnetic field, and the relationships between intensity and magnetic field of starspots. This results in the identification of specific free parameters influencing the trajectory of CMEs: the initial position, velocities, and the strength and configuration of the magnetic field.

3. Magnetic Background Parameters

Kay *et al.* (2013, 2015) introduced the ForeCAT model, designed for computing the deflection and rotation of a CME influenced by Lorentz force components – pressure gradient and tension of the magnetic field. The model calculates the three-dimensional (3D) trajectories of CMEs, capturing the fundamental patterns observed in actual CMEs. We use an older, slightly less complex version of ForeCAT than the one presented in Kay *et al.* (2022), since we do not consider an elliptical CME cross section in Menezes *et al.* (2023), given how little observational constraints there are on extrasolar CMEs. The model's input parameters encompass the CME and star characteristics, in addition to magnetograms.

The simulated CME, embedded in a magnetic background, undergoes deflection and rotation, affecting its position and orientation (Kay *et al.* 2019). Unlike more sophisticated MHD models, ForeCAT simplifies for accurate CME reproduction, using a static solar magnetic field model to determine the magnetic tension and pressure gradient, resulting from the stellar background magnetic field, B_{SW} (Kay *et al.* 2015).

Stellar magnetograms are used as input to determine the B_{SW} at a source-surface height (described further) using a PFSS model (Altschuler and Newkirk 1969; Schatten *et al.* 1969). For the solar simulations we use a synoptic photospheric magnetograms of the Carrington rotation CR2203[†] generated by SDO/HMI (Pesnell *et al.* 2012; Scherrer *et al.* 2012). Nonetheless, there are no magnetograms available for Kepler-63 nor Kepler-411, not even magnetograms reconstructed by the Zeeman–Doppler Imaging technique (ZDI; Donati and Brown 1997; Vidotto *et al.* 2012, 2013, 2015; Yu *et al.* 2017). Thus, we reconstructed magnetograms for the Kepler-63 and Kepler-411, by extrapolating the magnetic field of the starspots based on their intensity and positions obtained from spot transit mapping performed by Netto and Valio (2020) and Araújo and Valio (2021), respectively.

Silva (2003) demonstrated the characterization of surface features on solar-like stars through planetary transits. During a transit, a planet may occult starspots, causing detectable variations in the light curve. Improved versions of this model allow the inference of starspot physical properties, including size, intensity, position, and temperature (Valio *et al.* 2017; Zaleski *et al.* 2019; Netto and Valio 2020; Zaleski *et al.* 2020; Selhorst *et al.* 2020; Araújo and Valio 2021; Zaleski *et al.* 2022). Using SOHO/MDI data, Valio *et al.* (2020) established linear fits for magnetic field (B) as a function of spot intensity, differentiating between warm and cold spots, however in Menezes *et al.* (2023), we simplified this relation to a single equation.

Then, from the position, intensity and size of the starspots of Kepler-63 and Kepler-411, we were able to reconstruct magnetograms for these stars. Since there was a great number of starspots mapped in both stars, we develop a method to choose maps with most intense magnetic field intensity and flux. These selected maps had their starspots transformed into horizontal dipoles, with the rest of the map filled with a scaled solar magnetogram.

[†] 2018-04-19 05:10 – 2018-05-16 10:53 UTC (solar minimum)

Table 1. Total magnetic flux of each stellar model.

Star	$ \Phi _{\text{total}}$ (Mx)
Sun	1.13×10^{25}
Kepler-63	5.23×10^{25}
Kepler-411	3.90×10^{25}

Additionally, the multiplication factors for adjusting the solar magnetogram are discussed, taking into account the mean magnetic field strengths of the sunspots in each star’s model. Menezes et al. (2023) provides more details on such methods. Table 1 lists the total magnetic flux of each stellar model.

Despite the fact that dynamo-age relationship is not linearly proportional, we considered this a reasonable hypothesis. Reconstructed magnetograms for Kepler-63 and Kepler-411 indicate total magnetic flux values ($|\Phi|_{\text{total}}$) of 5.23×10^{25} and 3.90×10^{25} Mx, respectively. A study by Coffaro et al. (2022) measured the X-ray luminosity ($\log L_X$) for Kepler-63 as approximately 29, suggesting a $|\Phi|_{\text{total}}$ of around 10^{25} Mx using the relation between average surface magnetic flux and X-ray luminosity. This reconstructed value closely aligns with the one obtained in this work.

By utilizing stellar magnetograms, one can compute the magnetic force fields generated by B_{SW} through the PFSS model. We generated the maps of B_{SW} for all simulations at $R_{\text{SS}} = 2.5 R_\star$, and their respective deflection force fields, with the PFSS model.

Figure 1 summarizes the process of mapping stellar spots, reconstructing magnetograms, calculating B_{SW} , and extrapolating magnetic field lines, along with 3D visualizations of the respective maps. In the case of the Sun, the intensity map normalized by the flux at the center of the solar disk, $F_{\star, \text{ctr}}$, serves only as an illustration, as its magnetogram was directly generated from SDO/HMI data. The figure shows 3D visualizations of starspot intensity maps (top row), magnetograms (second row), B_{SW} at $2, 5 R_\star$ (third row), and extrapolated magnetic field lines (bottom row). The color scales represent intensity (normalized by $F_{\star, \text{ctr}}$) and magnetic field strength (in G). The left column panels correspond to the Sun; the center column panels correspond to Kepler-63; the right column panels correspond to Kepler-411. It is worth noting that B_{SW} maps, tend to approach the Astrospheric Current Sheet shape, and have higher intensities located at the poles due to coronal holes.

4. CME and Stellar Parameters

Kay et al. (2015) describes the model’s CME geometry as a 3D rigid half torus, representing the flux rope’s behavior as a function of radial distance. While CMEs may undergo deformation and erosion during propagation (Savani et al. 2011; Riley and Crooker 2004; Riley et al. 2004; Nieves–Chinchilla et al. 2018), observations and simulations indicate that they generally keep this shape up to 1 AU (Burlaga et al. 1981; Klein and Burlaga 1982; Cane and Richardson 2003; Vandas et al. 2002). In Menezes et al. (2023) the shape parameters, grid points and initial inclination (inc_o , measured clockwise from the equatorial plane) are kept the same for all simulations.

Other important initial CME parameters are angular width (size), mass, and velocity. Empirical models determine these parameters as functions of radial distance (Kay et al. 2013, 2015, 2016; Menezes et al. 2023). The CME trajectories are simulated from $1.1 R_\star$ to $160 R_\star$, since after this point the deflections are very low or null, keeping the trajectories stable. The parameters to calculate angular width and mass over radial propagation are the same for all simulations, however for velocity we used 3 configurations: low-velocity with initial velocity of $v_o = 50$ km/s and final velocity of $v_f = 400$ km/s, mid-velocity

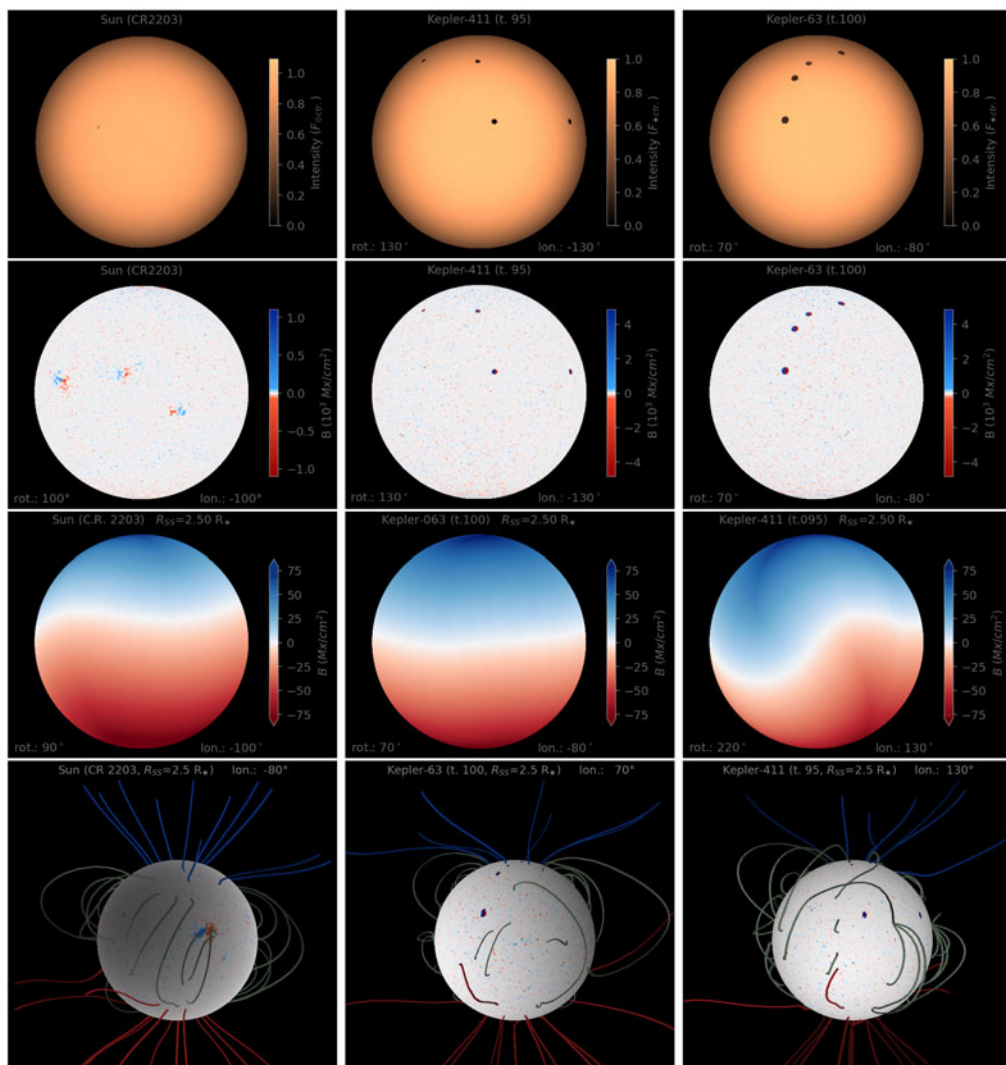


Figure 1. 3D visualizations of starspot intensity maps (top row), magnetograms (second row), B_{SW} at $2.5 R_*$ (third row), and extrapolated magnetic field lines (bottom row). The color scales represent intensity (normalized by $F_{\text{star,ctr}}$) and magnetic field strength (in G). The left column panels correspond to the Sun; the center column panels correspond to Kepler-63; the right column panels correspond to Kepler-411.

with $v_o = 70 \text{ km/s}$ and $v_f = 650 \text{ km/s}$, and high-velocity with $v_o = 90 \text{ km/s}$ and $v_f = 900 \text{ km/s}$.

Finally, the other free parameters are the initial latitude, lat_o , and longitude, lon_o , of the CMEs. The initial position (lon_o , lat_o , inc_o) of the CME is based on regions of concentrated B field, lining up the torus with polarity inversion lines, locations where flux ropes would be likely to form. We set 3 different values of lat_o for each model, so that there are low-, mid- and high-latitude configuration. In Table 2, we list the starting position of CMEs for all simulations.

The stellar radius, R_* , and rotation rate, Ω_* , also must be set. As stated in Menezes *et al.* (2023), for the Sun the values are respectively $7.0 \times 10^{10} \text{ cm}$ and $2.8 \times 10^{-6} \text{ rad/s}$; for Kepler-63, $6.3 \times 10^{10} \text{ cm}$ and $1.3 \times 10^{-5} \text{ rad/s}$ (Sanchis-Ojeda *et al.*

Table 2. Initial position of CMEs for each star model and latitudinal region.

Region	Sun		Kepler-63		Kepler-411	
	lat _o	lon _o	lat _o	lon _o	lat _o	lon _o
High	45,0°	70,0°	47,6°	97,8°	49,3°	48,9°
Mid	30,0°	70,0°	36,9°	89,3°	30,0°	80,0°
Low	10,0°	70,0°	11,8°	86,5°	11,1°	110,4°

2013; Netto and Valio 2020); and for Kepler-411, 5.5×10^{10} cm and 6.9×10^{-6} rad/s (Araújo and Valio 2021). The model calculates the non-radial drag effects between a CME and the solar wind, using and adapted of the expression of Cargill et al. (1996) and Cargill (2004), with drag coefficient of $C_d = 1$.

5. Results, Discussion and Conclusions

Our work focuses on unraveling CME trajectories influenced by different stellar magnetic backgrounds (Menezes et al. 2023). We reconstructed photospheric magnetograms for the solar-like stars Kepler-63 and Kepler-411 by extrapolating the magnetic field (B) of their respective mapped starspots (Valio et al. 2020; Netto and Valio 2020; Araújo and Valio 2021), and then computed the B_{SW} maps for all stellar models. We performed 27 simulations of CME trajectories for the Sun, Kepler-63, and Kepler-411, using the ForeCAT model. All simulations shared identical input parameters, except for initial positions (\mathbf{lon}_o and \mathbf{lat}_o), velocities (v_o and v_f), stellar parameters (R_\star and Ω_\star), and background magnetic fields, B_{SW} . Furthermore, we calculated the total variations of longitude, Δlon , latitude, Δlat , and rotation, Δrot , over the complete CME trajectories ($1.1 - 160 R_\star$) – final position values minus initial position values. In Figure 2, the total variations are listed by star, initial latitude, and velocities.

The most intense longitude deflections occur within approximately $2 R_\star$, with rotation exhibiting more intense variations near the stellar surface. Latitude deflections are most pronounced in the solar model for low latitudes, up to about $3 R_\star$, and in the Kepler-63 models for both low and mid latitudes, up to approximately $2 R_\star$. In other simulations, latitude deflections are more significant up to around $6 R_\star$, after which they persist with lower values. This behavior is attributed to the influence of concentrated magnetic field regions, such as spots or active regions, leading to CME trajectory deflection and rotation closer to the stellar photosphere (Kay et al. 2013, 2015; Menezes et al. 2023).

The latitude variations follow a gradual trend along the propagation, aligning with the approach of the Astrospheric Current Sheet by the solar wind, and CMEs tend to deviate toward regions of minimal magnetic energy. Although low-latitude solar simulations exhibit more intense latitude deflections up to around $2 R_\star$, the absolute values of total latitude variations (Δlat) are very low, less than 1° . In contrast, Kepler-63 simulations show more significant Δlat values, ranging from approximately 13° to 17° for low-latitude simulations and 56° to 95° for mid-latitude simulations.

All CMEs generally exhibit latitude variations toward the Astrospheric Current Sheet, except for Kepler-63 mid-latitude simulations. The magnetic forces responsible for CME deflection decay rapidly over radial distance, resulting in most deflection and rotation occurring near the stellar surface. The magnetic pressure gradient is the dominant force contributing to CME deflection toward the Astrospheric Current Sheet. However, intense magnetic fields of spots can cause greater deflection, leading to cases where CMEs propagate toward high latitudes.

The absolute total variations in deflections and rotations are small for solar simulations, intermediate for Kepler-411 simulations, and intense in Kepler-63 model. This trend agrees with the photospheric magnetic field flux of the stars Table 1. Kepler-63

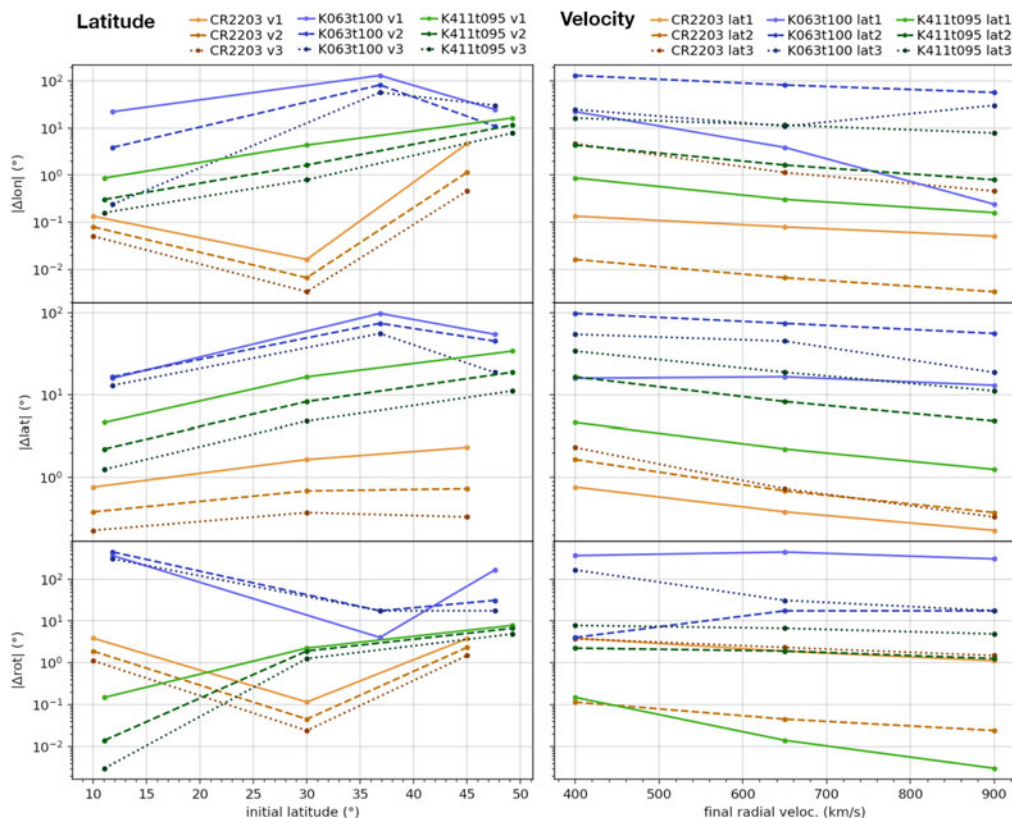


Figure 2. Total variations of the simulated CME trajectories in longitude, Δlon , latitude, Δlat , and rotation, Δrot , as functions of initial latitudes (lat_0 , left panels) and final velocities (v_f , right panels). In both columns, the colors represent the simulations of the Sun (orange), Kepler-63 (blue), and Kepler-411 (green). In the left panels, the solid, dashed and dotted lines represent respectively low-, mid- and high-latitudes simulations. In the right panels the same as the left, but respectively for velocities.

simulations show significantly larger CME deflections and rotations compared to solar CMEs, driven by the stronger ambient magnetic field and more concentrated magnetic field in active regions. The absolute total variations of deflections and rotations increase with initial latitudes, influenced by concentrated field regions and the tendency of CMEs to deviate toward the Astrospheric Current Sheet. In most cases, Δlon , Δlat , and Δrot are inversely proportional to initial and final velocities (v_0 and v_f). However, Kepler-63 simulations exhibit deviations from these trends, attributed to the unique spatial configuration of large spots on its surface.

Kay *et al.* (2016) reported that planets with orbits closely aligned with the equatorial plane of their host stars are more susceptible to being impacted by CMEs. However in our work, Kepler-63's CMEs of mid-latitude and low- to mid-velocities were ejected from the northern hemisphere, deflecting their trajectory toward the south pole. Given Kepler-63b's near polar orbit (Sanchis-Ojeda *et al.* 2013; Netto and Valio 2020), the likelihood of it being affected by CMEs increases. Another intriguing feature of this star is the presence of a large and long-lived polar spot (Sanchis-Ojeda *et al.* 2013), prompting consideration of whether it serves as a CME overproducing region. Considering the elevated latitudes and the tendency for high-velocity CMEs to follow more radial trajectories, Kepler-63b emerges as a potential frequent target for CME impacts. Additionally, it is noteworthy

that although active stars may theoretically generate numerous CMEs (directed towards the poles, as observed in Kepler-63, or deflected to the Astrospheric Current Sheet, as seen in Kepler-411), the robust magnetic field could prevent CME eruption through magnetic confinement (Alvarado-Gómez et al. 2018; Sun et al. 2022), thereby diminishing CME detection rates.

The impact of CMEs on space weather near planets depends of factors such as CME rotation and the direction of its B field. The direction of the B field resulting from the CME is crucial, as similar directions tend to cause compression in a planet's B field, while opposite directions can lead to significant changes through reconnection. The simulations indicate that the rotational displacement (Δ_{rot}) of CMEs is highest in the case of Kepler-63, with some CMEs rotating more than 360 degrees.

Overall, more homogeneous magnetic field, like that of the Sun, results in CMEs with lower deflections, while a magnetogram like that of Kepler-63 generates less stable trajectories. Additionally, the velocity of CMEs influences their trajectories, with faster CMEs exhibiting less deflections on their trajectories. The current understanding of stellar CMEs is still incipient, and despite using certain approximations and hypotheses, simulations for Kepler-63 and Kepler-411 were conducted. The findings indicate that free parameters, such as velocity, latitude, and specially magnetic topology, significantly affect CME trajectories. In the future we intend to explore additional parameters like initial inclination, angular width, and mass of CMEs, as well as using different magnetic backgrounds for different star models.

Acknowledgements F. M. acknowledges financial support from the Fundo Mackenzie de Pesquisa e Inovação (MackPesquisa), the Coordenação de Aperfeiçoamento de Pessoal de Nível Superior (CAPES), and the Fundação de Amparo à Pesquisa do Estado de São Paulo (FAPESP; process numbers 2022/12024-0 and 2013/10559-5). A. A. acknowledges financial support from the Conselho Nacional de Desenvolvimento Científico e Tecnológico (CNPq; #150817/2022-3). The CR2203 synoptic photospheric magnetograms is a courtesy of NASA/SDO and the AIA, EVE, and HMI science teams.

References

- M. D. Altschuler and G. Newkirk. *Solar Physics*, 9(1):131–149, Sept. 1969. DOI: 10.1007/BF00145734.
- J. D. Alvarado-Gómez, J. J. Drake, O. Cohen, S. P. Moschou, and C. Garraffo. *Astrophysical Journal*, 862(2):93, Aug. 2018. DOI: 10.3847/1538-4357/aac77f.
- A. Araújo and A. Valio. *Astrophysical Journal Letters*, 907(1):L5, Jan. 2021. DOI: 10.3847/2041-8213/abd3a7.
- S. V. Berdyugina. *Living Reviews in Solar Physics*, 2(1):8, Dec. 2005. DOI: 10.12942/lrsp-2005-8.
- A. S. Brun and M. K. Browning. *Living Reviews in Solar Physics*, 14(1):4, Sept. 2017. DOI: 10.1007/s41116-017-0007-8.
- L. Burlaga, E. Sittler, F. Mariani, and R. Schwenn. *Journal of Geophysical Research*, 86(A8): 6673–6684, Aug. 1981. DOI: 10.1029/JA086iA08p06673.
- H. V. Cane and I. G. Richardson. *Journal of Geophysical Research (Space Physics)*, 108(A4): 1156, Apr. 2003. DOI: 10.1029/2002JA009817.
- P. J. Cargill. *Solar Physics*, 221(1):135–149, May 2004. DOI: 10.1023/B:SOLA.0000033366.10725.a2.
- P. J. Cargill, J. Chen, D. S. Spicer, and S. T. Zalesak. *Journal of Geophysical Research*, 101 (A3):4855–4870, Mar. 1996. DOI: 10.1029/95JA03769.
- P. Charbonneau. *Annual Review of Astron. Astrophys*, 52:251–290, Aug. 2014. DOI: 10.1146/annurev-astro-081913-040012.
- M. Coffaro, B. Stelzer, and S. Orlando. *Astronomy and Astrophysics*, 661:A79, May 2022. DOI: 10.1051/0004-6361/202142298.

- H. Cremades and V. Bothmer. *Astronomy and Astrophysics*, 422:307–322, July 2004. DOI: 10.1051/0004-6361:20035776.
- J. F. Donati and S. F. Brown. *Astronomy and Astrophysics*, 326:1135–1142, Oct. 1997.
- R. Estrela and A. Valio. *Astrophysical Journal*, 831:57, Nov. 2016. DOI: 10.3847/0004-637X/831/1/57.
- R. Estrela and A. Valio. *Astrobiology*, 18(11):1414–1424, Nov 2018. DOI: 10.1089/ast.2017.1724.
- R. Estrela, S. Palit, and A. Valio. *Astrobiology*, 20(12):1465–1475, Dec. 2020. DOI: 10.1089/ast.2019.2126.
- N. Gopalswamy, S. Yashiro, G. Michalek, G. Stenborg, A. Vourlidas, S. Freeland, and R. Howard. *Earth Moon and Planets*, 104(1-4):295–313, Apr. 2009. DOI: 10.1007/s11038-008-9282-7.
- M. Guhathakurta, E. C. Sittler, and L. Ofman. *Journal of Geophysical Research (Space Physics)*, 111(A11):A11215, Nov. 2006. DOI: 10.1029/2006JA011931.
- A. Izidoro, M. Ogihara, S. N. Raymond, A. Morbidelli, A. Pierens, B. Bitsch, C. Cossou, and F. Hersant. *Monthly Notices of the Royal Astronomical Society*, 470(2):1750–1770, Sept. 2017. DOI: 10.1093/mnras/stx1232.
- C. Kay, M. Opher, and R. M. Evans. *Astrophysical Journal*, 775(1):5, Sep 2013. DOI: 10.1088/0004-637X/775/1/5.
- C. Kay, M. Opher, and R. M. Evans. *Astrophysical Journal*, 805(2):168, Jun 2015. DOI: 10.1088/0004-637X/805/2/168.
- C. Kay, M. Opher, and M. Kornbleuth. *Astrophysical Journal*, 826(2):195, Aug 2016. DOI: 10.3847/0004-637X/826/2/195.
- C. Kay, V. S. Airapetian, T. Lüftinger, and O. Kochukhov. *Astrophysical Journal Letters*, 886(2):L37, Dec. 2019. DOI: 10.3847/2041-8213/ab551f.
- C. Kay, M. L. Mays, and Y. M. Collado-Vega. *Space Weather*, 20(4):e02914, Apr. 2022. DOI: 10.1029/2021SW002914.
- E. K. J. Kilpua, J. Pomoell, A. Vourlidas, R. Vainio, J. Luhmann, Y. Li, P. Schroeder, A. B. Galvin, and K. Simunac. *Annales Geophysicae*, 27(12):4491–4503, Dec. 2009. DOI: 10.5194/angeo-27-4491-2009.
- L. W. Klein and L. F. Burlaga. *Journal of Geophysical Research*, 87(A2):613–624, Feb. 1982. DOI: 10.1029/JA087iA02p00613.
- P. Lang, M. Jardine, J. Morin, J.-F. Donati, S. Jeffers, A. A. Vidotto, and R. Fares. *Monthly Notices of the Royal Astronomical Society*, 439:2122–2131, Apr. 2014. DOI: 10.1093/mnras/stu091.
- R. M. MacQueen, A. J. Hundhausen, and C. W. Conover. *Journal of Geophysical Research*, 91(A1):31–38, Jan. 1986. DOI: 10.1029/JA091iA01p00031.
- F. Menezes, C. L. Selhorst, C. G. Giménez de Castro, and A. Valio. *Astrophysical Journal*, 910(1):77, Mar. 2021. DOI: 10.3847/1538-4357/abe41c.
- F. Menezes, A. Valio, Y. Netto, A. Araújo, C. Kay, and M. Opher. *Monthly Notices of the Royal Astronomical Society*, 522(3):4392–4403, July 2023. DOI: 10.1093/mnras/stad1078.
- B. M. Morris. *Astrophysical Journal*, 893(1):67, Apr. 2020. DOI: 10.3847/1538-4357/ab79a0.
- Y. Netto and A. Valio. *Astronomy and Astrophysics*, 635:A78, Mar. 2020. DOI: 10.1051/0004-6361/201936219.
- T. Nieves-Chinchilla, M. G. Linton, M. A. Hidalgo, and A. Vourlidas. *Astrophysical Journal*, 861(2):139, July 2018. DOI: 10.3847/1538-4357/aac951.
- E. N. Parker. *Astrophysical Journal*, 122:293, Sept. 1955. DOI: 10.1086/146087.
- W. D. Pesnell, B. J. Thompson, and P. C. Chamberlin. *Solar Physics*, 275(1-2):3–15, Jan. 2012. DOI: 10.1007/s11207-011-9841-3.
- P. Riley and N. U. Crooker. *Astrophysical Journal*, 600(2):1035–1042, Jan. 2004. DOI: 10.1086/379974.
- P. Riley, J. A. Linker, R. Lionello, Z. Mikić, D. Odstrcil, M. A. Hidalgo, C. Cid, Q. Hu, R. P. Lepping, B. J. Lynch, and A. Rees. *Journal of Atmospheric and Solar-Terrestrial Physics*, 66(15-16):1321–1331, Oct. 2004. DOI: 10.1016/j.jastp.2004.03.019.
- R. Sanchis-Ojeda, J. N. Winn, G. W. Marcy, A. W. Howard, H. Isaacson, J. A. Johnson, G. Torres, S. Albrecht, T. L. Campante, W. J. Chaplin, G. R. Davies, M. N. Lund, J. A.

- Carter, R. I. Dawson, L. A. Buchhave, M. E. Everett, D. A. Fischer, J. C. Geary, R. L. Gilliland, E. P. Horch, S. B. Howell, and D. W. Latham. *Astrophysical Journal*, 775(1): 54, Sep 2013. DOI: 10.1088/0004-637X/775/1/54.
- N. P. Savani, M. J. Owens, A. P. Rouillard, R. J. Forsyth, K. Kusano, D. Shiota, and R. Kataoka. *Astrophysical Journal*, 731(2):109, Apr. 2011. DOI: 10.1088/0004-637X/731/2/109.
- K. H. Schatten, J. M. Wilcox, and N. F. Ness. *Solar Physics*, 6(3):442–455, Mar. 1969. DOI: 10.1007/BF00146478.
- P. H. Scherrer, J. Schou, R. I. Bush, A. G. Kosovichev, R. S. Bogart, J. T. Hoeksema, Y. Liu, T. L. Duvall, J. Zhao, A. M. Title, C. J. Schrijver, T. D. Tarbell, and S. Tomczyk. *Solar Physics*, 275(1-2):207–227, Jan. 2012. DOI: 10.1007/s11207-011-9834-2.
- C. L. Selhorst, C. L. Barbosa, P. J. A. Simões, A. A. Vidotto, and A. Valio. *Astrophysical Journal*, 895(1):62, May 2020. DOI: 10.3847/1538-4357/ab89a4.
- A. V. R. Silva. *Astrophysical Journal Letters*, 585:L147–L150, Mar. 2003. DOI: 10.1086/374324.
- A. Skumanich. *Astrophysical Journal*, 171:565, Feb. 1972. DOI: 10.1086/151310.
- H. Spruit. *Memorie della Società Astronomia Italiana*, 68:397, 1997.
- H. C. Spruit, G. B. Scharmer, and M. G. Löfdahl. *Astronomy and Astrophysics*, 521:A72, Oct. 2010. DOI: 10.1051/0004-6361/200912519.
- A. M. Stejko, G. Guerrero, A. e. G. Kosovichev, and P. K. Smolarkiewicz. *Astrophysical Journal*, 888(1):16, Jan. 2020. DOI: 10.3847/1538-4357/ab5854.
- L. Sun, P. Ioannidis, S. Gu, J. H. M. M. Schmitt, X. Wang, and M. B. N. Kouwenhoven. *Astronomy and Astrophysics*, 624:A15, Apr. 2019. DOI: 10.1051/0004-6361/201834275.
- X. Sun, T. Török, and M. L. DeRosa. *Monthly Notices of the Royal Astronomical Society*, 509(4):5075–5085, Feb. 2022. DOI: 10.1093/mnras/stab3249.
- A. Valio, R. Estrela, Y. Netto, J. P. Bravo, and J. R. de Medeiros. *Astrophysical Journal*, 835: 294, Feb. 2017. DOI: 10.3847/1538-4357/835/2/294.
- A. Valio, E. Spaggiari, M. Marengoni, and C. L. Selhorst. *Solar Physics*, 295(9):120, Sept. 2020. DOI: 10.1007/s11207-020-01691-3.
- M. Vandas, D. Odstrčil, and S. Watari. *Journal of Geophysical Research (Space Physics)*, 107(A9):1236, Sept. 2002. DOI: 10.1029/2001JA005068.
- A. A. Vidotto, M. Jardine, M. Opher, J. F. Donati, and T. I. Gombosi. *Monthly Notices of the Royal Astronomical Society*, 412(1):351–362, Mar. 2011. DOI: 10.1111/j.1365-2966.2010.17908.x.
- A. A. Vidotto, R. Fares, M. Jardine, J.-F. Donati, M. Opher, C. Moutou, C. Catala, and T. I. Gombosi. *Monthly Notices of the Royal Astronomical Society*, 423:3285–3298, July 2012. DOI: 10.1111/j.1365-2966.2012.21122.x.
- A. A. Vidotto, M. Jardine, J. Morin, J.-F. Donati, P. Lang, and A. J. B. Russell. *Astronomy and Astrophysics*, 557:A67, Sept. 2013. DOI: 10.1051/0004-6361/201321504.
- A. A. Vidotto, M. Jardine, J. Morin, J. F. Donati, M. Opher, and T. I. Gombosi. *Monthly Notices of the Royal Astronomical Society*, 438:1162–1175, Feb. 2014. DOI: 10.1093/mnras/stt2265.
- A. A. Vidotto, R. Fares, M. Jardine, C. Moutou, and J.-F. Donati. *Monthly Notices of the Royal Astronomical Society*, 449:4117–4130, June 2015. DOI: 10.1093/mnras/stv618.
- B. E. Wood, H.-R. Müller, G. P. Zank, and J. L. Linsky. *Astrophysical Journal*, 574(1):412–425, July 2002. DOI: 10.1086/340797.
- L. Yu, J.-F. Donati, E. M. Hébrard, C. Moutou, L. Malo, K. Grankin, G. Hussain, A. Collier Cameron, A. A. Vidotto, C. Baruteau, S. H. P. Alencar, J. Bouvier, P. Petit, M. Takami, G. Herczeg, S. G. Gregory, M. Jardine, J. Morin, F. Ménard, and Matysse Collaboration. *Monthly Notices of the Royal Astronomical Society*, 467:1342–1359, May 2017. DOI: 10.1093/mnras/stx009.
- S. M. Zaleski, A. Valio, S. C. Marsden, and B. D. Carter. *Monthly Notices of the Royal Astronomical Society*, 484(1):618–630, Mar. 2019. DOI: 10.1093/mnras/sty3474.
- S. M. Zaleski, A. Valio, B. D. Carter, and S. C. Marsden. *Monthly Notices of the Royal Astronomical Society*, 492(4):5141–5151, Mar. 2020. DOI: 10.1093/mnras/staa103.
- S. M. Zaleski, A. Valio, B. D. Carter, and S. C. Marsden. *Monthly Notices of the Royal Astronomical Society*, 510(4):5348–5361, Mar. 2022. DOI: 10.1093/mnras/stab3788.